Article

Growth Mechanism of Periodic-Structured MoS$_2$ by Transmission Electron Microscopy

Arvind Mukundan [1], Yu-Ming Tsao [1], Sofya B. Artemkina [2,3], Vladimir E. Fedorov [2,3] and Hsiang-Chen Wang [1,*]

[1]   Department of Mechanical Engineering, Advanced Institute of Manufacturing with High Tech Innovations (AIM-HI), and Center for Innovative Research on Aging Society (CIRAS), National Chung Cheng University, 168, University Rd., Min Hsiung, Chia Yi 62102, Taiwan; d09420003@ccu.edu.tw (A.M.); d09420002@ccu.edu.tw (Y.-M.T.)
[2]   Nikolaev Institute of Inorganic Chemistry, Siberian Branch of Russian Academy of Sciences, 630090 Novosibirsk, Russia; artem@niic.nsc.ru (S.B.A.); fed@niic.nsc.ru (V.E.F.)
[3]   Department of Natural Sciences, Novosibirsk State University, 1 Pirogova Str., 630090 Novosibirsk, Russia
*   Correspondence: hcwang@ccu.edu.tw

Abstract: Molybdenum disulfide (MoS$_2$) was grown on a laser-processed periodic-hole sapphire substrate through chemical vapor deposition. The main purpose was to investigate the mechanism of MoS$_2$ growth in substrate with a periodic structure. By controlling the amount and position of the precursor, adjusting the growth temperature and time, and setting the flow rate of argon gas, MoS$_2$ grew in the region of the periodic holes. A series of various growth layer analyses of MoS$_2$ were then confirmed by Raman spectroscopy, photoluminescence spectroscopy, and atomic force microscopy. Finally, the growth mechanism was studied by transmission electron microscopy (TEM). The experimental results show that in the appropriate environment, MoS$_2$ can be successfully grown on substrate with periodic holes, and the number of growth layers can be determined through measurements. By observing the growth mechanism, composition analysis, and selected area electron diffraction diagram by TEM, we comprehensively understand the growth phenomenon. The results of this research can serve as a reference for the large-scale periodic growth of MoS$_2$. The production of periodic structures by laser drilling is advantageous, as it is relatively simpler than other methods.

Keywords: chemical vapor deposition; periodic growth of MoS$_2$; growth mechanism of MoS$_2$; Molybdenum disulfide (MoS$_2$)

1. Introduction

One of the most important two-dimensional (2D) transition metal chalcogenides that is gaining increased attention is MoS$_2$ [1–7]. Materials with nanoscale electronic and optoelectronic components, such as field-effect transistors, prospective memory components, light-emitting diodes, and sensors, have been manufactured by exploiting the excellent spin–valley coupling and flexural and optoelectronic properties of MoS$_2$ [8–20]. Two-dimensional MoS$_2$ is low cost and does not require complex preparation [21]. To date, MoS$_2$-based semiconductor heterostructures, such as CdS/MoS$_2$, MoO$_3$/MoS$_2$, and SnO$_2$/MoS$_2$, featuring good photocatalytic or photoelectrochemical properties, have been successfully synthesized owing to the efficient charge separation obtained by coupling two semiconductor structures with matched energy levels [22–25]. Nevertheless, the mass production of such devices demands a method of synthesizing large-scale, layer-controlled, high-quality MoS$_2$. Most studies on MoS$_2$ films with excellent results have been obtained using a top-down approach, such as mechanical exfoliation [26,27]. Other studies are moving from characterizing 2D thin films to manufacturing low-cost devices, mass producing logic-integrated circuits, and growing 2D materials on foreign substrates. They aim to replace the existing exfoliation and liquid exfoliation methods for producing randomly distributed flakes and

providing limited control of the number of MoS_2 film layers. Chemical vapor deposition (CVD) is the usual vapor-phase growth method used to create semiconductor thin films and heterojunctions [28]. CVD is gaining increased attention owing to its success in the growth of large-area, high-quality, and uniform nanofilms [29–33]. In the present work, MoS_2 was grown on a laser-processed periodic-hole sapphire substrate through the CVD method. We aimed to analyze the growth mechanism of MoS_2 with a regular structure by controlling the amount and location of the precursor, modifying the growth temperature and time, and setting the flow rate of argon gas (Ar) to induce MoS_2 growth around the periodic holes.

2. Materials and Methods

2.1. Preparation of Laser Drilling for Substrates Containing Periodic Structures

The most direct way to prepare many periodic patterned microstructures is to prepare traces on the substrate surface and to use laser processing to drill holes with about 10 μm diameter and 300 nm depth. Laser drilling damages the substrate structure and causes unevenness around the hole, which has a certain degree of influence on the MoS_2 growth mechanism.

2.2. Growth of MoS_2 on Sapphire Substrate by CVD

The substrate used to grow MoS_2 was sapphire with silicon dioxide (SiO_2) on the surface (see Supplementary Materials Section 1 for obtaining the MoS_2 layers). Periodic holes were made by laser processing, and then CVD was performed. The precursors used were sulfur powder (S) with a purity of 99.98% and molybdenum oxide powder (MoO_3) with a purity of 99.95%. High-purity chemical powders were used to remove impurities remaining in the experimental cavity and affecting the CVD. It was also possible to grow single crystals with residual impurities. The chemical solvent used to clean the remaining chemical substances after each experiment was aqua regia. The concentrations of nitric acid and hydrochloric acid (HCl) used to prepare aqua regia were 37 vol.% and 68–69 vol.%, respectively. The quartz tube and ceramic crucible were cleaned inside the tubular thermal furnace with this solution (see Supplementary Materials Section 2.6 for tube furnaces). The quartz tube was regularly replaced according to the change in residual sulfur powder on the tube wall. The purpose was to reduce the impact of experimental environmental factors. The substrates, organic solvents, gases, and chemicals used are detailed in Table 1.

**Table 1.** List of substrates, organic solvents, gases, and chemicals used for MoS_2.

S powder	Weiss Enterprise
MoO3 powder	Weiss Enterprise
Nitric acid	CHONEYE
Hydrochloric acid	FLUKA
Sapphire substrate	Vertex Co., Ltd.

Before the start of the experiment, the cleanliness of the substrate was confirmed (Supplementary Materials Section 2). First, 1 g of sulfur and 0.003 g of MoO_3 were prepared and placed in appropriate positions in the inner tube of the quartz tube. The substrate was set inverted on molybdenum trioxide (MoO_3). The inert gas used during growth was Ar. Initially, 500 sccm of Ar was let in for 10 min to clean the internal cavity. More water and oxygen were removed in the quartz tube, after which, the Ar flow was reduced to 200 sccm. The heating rate was set to 20 °C/min. The maximum temperature was set to 700 °C, and the heating time was set to 35 min. After reaching the maximum temperature, the same was maintained for 50 min. Finally, once the temperature dropped to <400 °C, it was further dropped to room temperature by opening the lid, and the MoS_2 structure was obtained. The experimental process is shown in Figure 1.
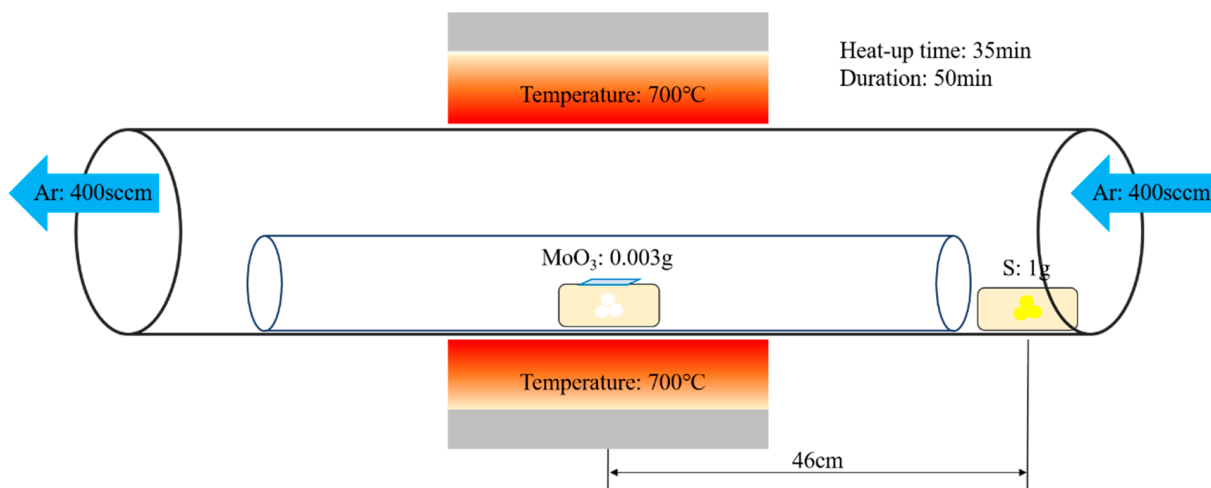
Figure 1. Flow chart of MoS$_2$ growth by CVD.

Considering that the vaporization point of MoO$_3$ is above 650 °C and the vaporization point of S is above 200 °C, MoO$_3$ in the gas phase underwent two chemical reactions in high-temperature environments to produce the intermediate molybdenum oxide (MoO$_{3-x}$). This intermediate molybdenum oxide diffused to the substrate and reacted with vaporized sulfur to form MoS$_2$ film. The distance between the two crucibles containing the precursor was 46 cm. Single-layer and multilayer MoS$_2$ can be effectively prepared by CVD, as shown in the following equations:

$$MoO_3(s) + H_2(g) \rightarrow MoO_2 + H_2O(g)$$

$$MoO_2(s) + 2S(g) \rightarrow MoS_2(s) + O_2(g)$$
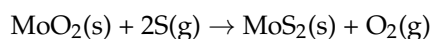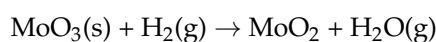
2.3. Growth Mechanism of MoS$_2$

The properties of MoS$_2$ are useful for semiconductors and optoelectronic materials with single or few layers. CVD is the most commonly used method for MoS$_2$ growth. Given that the location of CVD growth of single-layer MoS$_2$ is relatively random, understanding its growth mechanism can substantially benefit research on MoS$_2$ growth. TEM helps elucidate the atomic structure and the chemical composition information of particle evolution during catalysis [34–40]. The material properties of MoS$_2$ are preferably a single layer or very few layers. The analysis of the number of layers depended on the Raman spectra, atomic force microscopy (AFM) images, and photoluminescence (PL) spectra (see Supplementary Materials Section 2.1 for micro-Raman spectroscopy; see Supplementary Materials Section 2.2 for micro-Raman micro-PL spectrometer). Raman measurements were made using a laser with a wavelength of 532 nm as the excitation light source. TEM can also be used to measure the number of observation layers of the substrate cross-section (see Supplementary Materials Section 2.7 for transmission electron microscope). The multilayer structure in the cross-section geometry was studied by TEM using lamella specimens produced by focused ion beam (FIB) milling. The phase state of the multilayer volume was assessed by selected area electron diffraction (SAED) pattern analyses and fast Fourier transform (FFT) patterns generated from the corresponding regions of the HRTEM images (see Supplementary Materials Section 3 for TEM analysis).

3. Results

3.1. CVD Growth of Periodic MoS₂

The CVD method is used to grow MoS$_2$, and a substrate with periodic holes is prepared by laser drilling in a high-temperature furnace tube to grow MoS$_2$.

3.1.1. Image Analysis under Optical Microscopy (OM)

Many methods are well established to identify the number of MOS$_2$ layers, but in this study, an optical microscope was used (Supplementary Materials Section 2.3, optical microscope) [41–46]. OM reveals the growth pattern of MoS$_2$. Figure 2 shows the OM and SEM images of MoS$_2$ grown on a sapphire substrate.
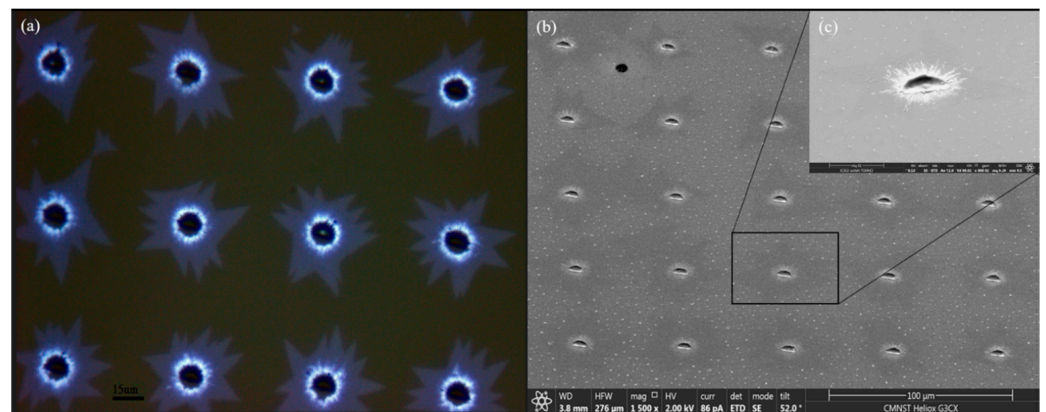
Figure 2. (**a**) OM image, (**b**) SEM image, and (**c**) partial enlarged view of (**b**) showing the periodic growth of MoS$_2$ on sapphire substrate.

Figure 3a is an image of the substrate after actual growth. The red arrow indicates the direction of Ar flow during CVD. The growth distributions of different MoS$_2$ shapes are shown as the marked locations b, c, d, and e. Figure 3b is the OM image at position b in Figure 3a, where the black holes are the result of the original laser processing, and the blue points are the areas where MoS$_2$ grows. Figure 3c is the OM image at position c in Figure 3a, where MoS$_2$ grows regularly in the hole area, with a bright blue ring pattern on the edge of the hole. This finding shows the existence of a multilayer MoS$_2$. The light blue irregular shape distribution on the periphery of the hole is represented by the existence of single-layer MoS$_2$. Figure 3d is the OM image at position d in Figure 3a, where we can see that a single layer of MoS$_2$ grows along the hole periphery. The periodic growth is not as good as that at the c position, but the single-layer MoS$_2$ covers a large area with no high-level MoS$_2$. Figure 3e is the OM image at position e in Figure 3a, where we can see that the single layer of MoS$_2$ grows in a more broken manner on the substrate and covers a larger area, but no MoS$_2$ exists around the hole. These results show that according to the Ar flow direction, MoS$_2$ grows in the order of large to small coverage area and from a broken and to a more regular growth around the hole until it no longer exists. Thus, we infer that the MoS$_2$ growth is cyclical.
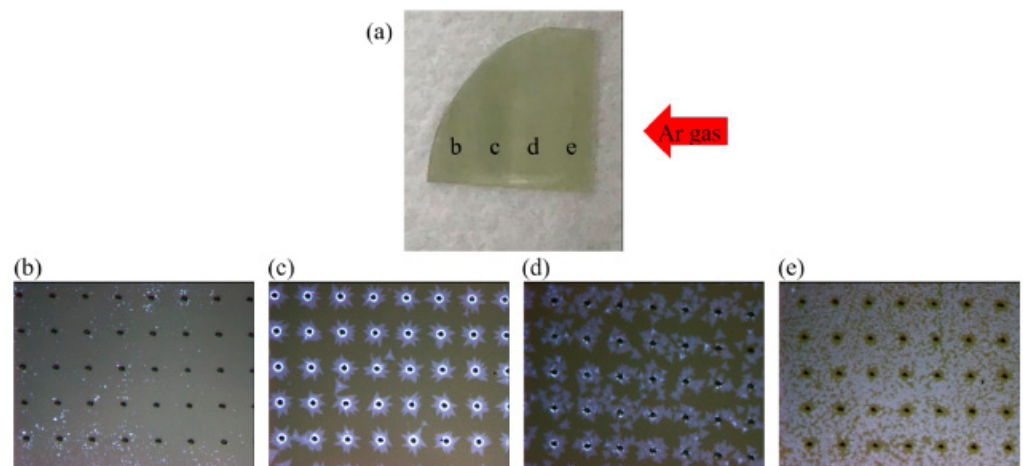
Figure 3. (**a**) Image of sapphire substrate after MoS$_2$ growth. (**b**) OM image at position b in (**a**). (**c**) OM image at position c in (**a**). (**d**) OM image at position d in (**a**), and (**e**) is the OM image at position e in (**a**).

3.1.2. Raman Spectrum Analysis Results

Raman mapping, which is the best method for analyzing the number of layers, is used to analyze the image [47–50]. The results reveal that MoS$_2$ has two peaks at 380 and 400 cm^{-1}, respectively. When the difference (Δk) between the two peaks is less than 20 cm^{-1}, it is a single-layer MoS$_2$ structure. The peak is attributed to the in-plane (E$_{12g}$) and out-of-plane (A$_{1g}$) oscillation modes of MoS$_2$.

Figure 4a shows an OM image of MoS$_2$ periodic growth. The black, blue, green, and red boxes indicate the areas where multilayer and one-, two-, and three-layer MoS$_2$ growth are measured, respectively. Figure 4b shows the Raman measurement diagram of each area marked in Figure 5a. The black part demonstrates that the Raman shift is between 384.7 and 408.8 cm^{-1}, and the value of the peak difference (Δk) is 24.1 cm^{-1}. This finding indicates more than four layers, which is unsuitable for semiconductor components and optoelectronic components. The blue part shows that the peak difference between the Raman shift of 386.2 and 405.3 cm^{-1} is 19.1 cm^{-1}, which represents a single layer. In the green part, we find that the peak difference between the Raman shift of 385.7 and 406.8 cm^{-1} is 21.1 cm^{-1}, defined as a two-layer growth of MoS$_2$. In the red part, we find that the peak difference between the Raman shift of 385.2 and 407.3 cm^{-1} is 22.1 cm^{-1}, defined as three layers of MoS$_2$. The Raman measurements prove that the periodicity of our growth has one- to three-layer and multilayer characteristics. These findings prove that MoS$_2$, which grows periodically in the hole, has different distributions from single to multiple layers and, thus, has multiple potential applications. The areas of few-layered MoS$_2$ are sufficiently large. Thus, it is highly applicable in semiconductor device manufacturing.

3.1.3. PL Spectrum Analysis Results

Figure 5a shows the result of the PL analysis of the MOS$_2$ sample. Obvious luminescence peaks exist at about 625 and 667 nm, indicating that MoS$_2$ is in a single layer and a few layers, respectively. Each layer corresponds with the valence band spin–orbit coupling splitting of MoS$_2$ direct exciton transition luminescence (B exciton) and direct energy gap recombination luminescence (A exciton). The converted energy is about 1.98 and 1.86 eV, respectively. We infer that this structure is single-layer MoS$_2$. Figure 5b shows the OM image of the selected PL mapping range. The greenish color is due to the light source of the instrument. Figure 5c shows the PL mapping diagram of the selected PL mapping range OM image with a wavelength of 625 nm in Figure 5b. The blue part is the sapphire substrate, and the yellow to red is the distribution from single layer to multilayer. The blue part is the sapphire substrate, and the yellow-orange to red is the distribution from single layer to multilayer. The dashed parts A and F correspond with the grid points of the *X*-axis position of the different color curves in Figure 5d. The color line segments A–F in the upper

right corner represent the number of grids selected in the *X*-axis direction of the mapping grid number 37 × 37 in Figure 5d. The positions of the line segments with higher strength are A, B, and C. A higher number of layers of growing MoS$_2$ corresponds with decreased strength, as shown in positions D, E, and F. From the results of the PL spectrum analysis, we infer from the mapping image presented by the excitation light peaks at 625 and 667 nm that the periodic growth of MoS$_2$ has good uniformity in the distribution of monolayer to multilayer.
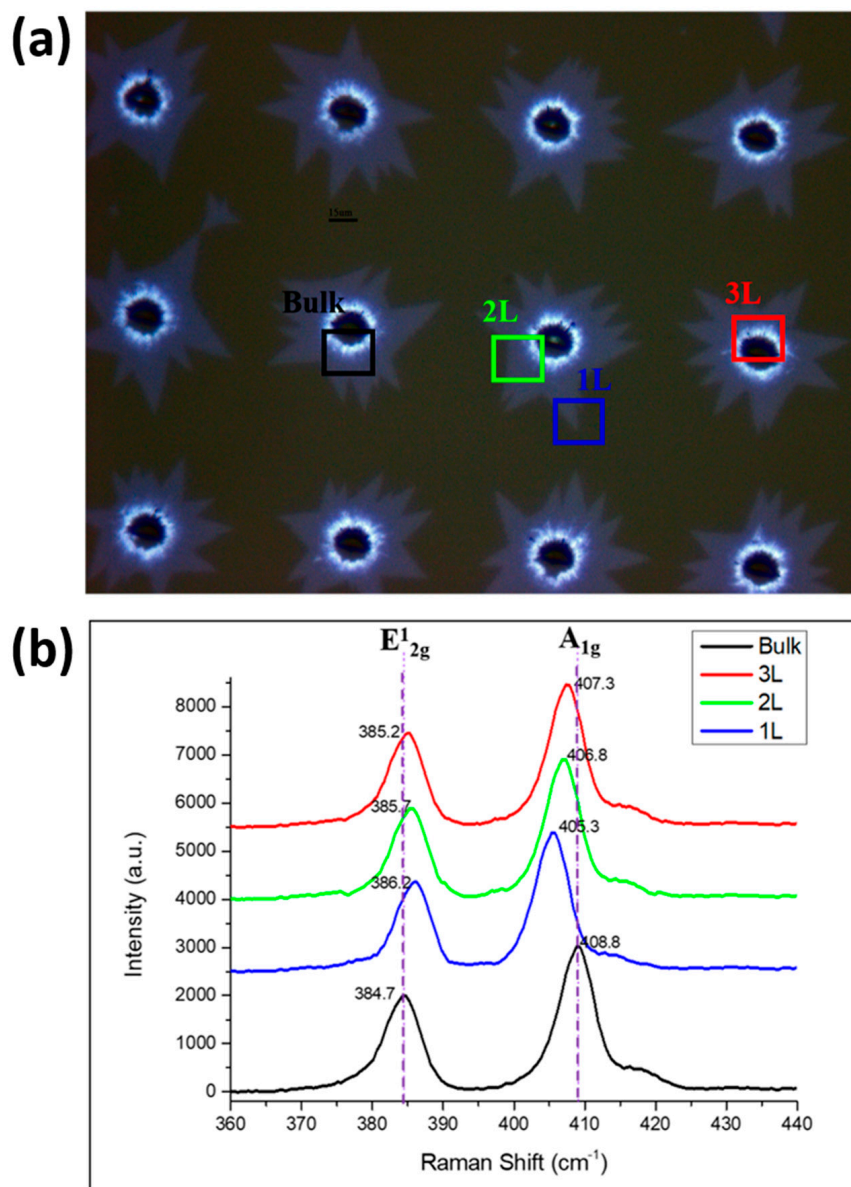

Figure 4. Panel (**a**) is an OM image of MoS$_2$ periodic growth, whereas (**b**) is the Raman measurement diagram of each area marked in (**a**).
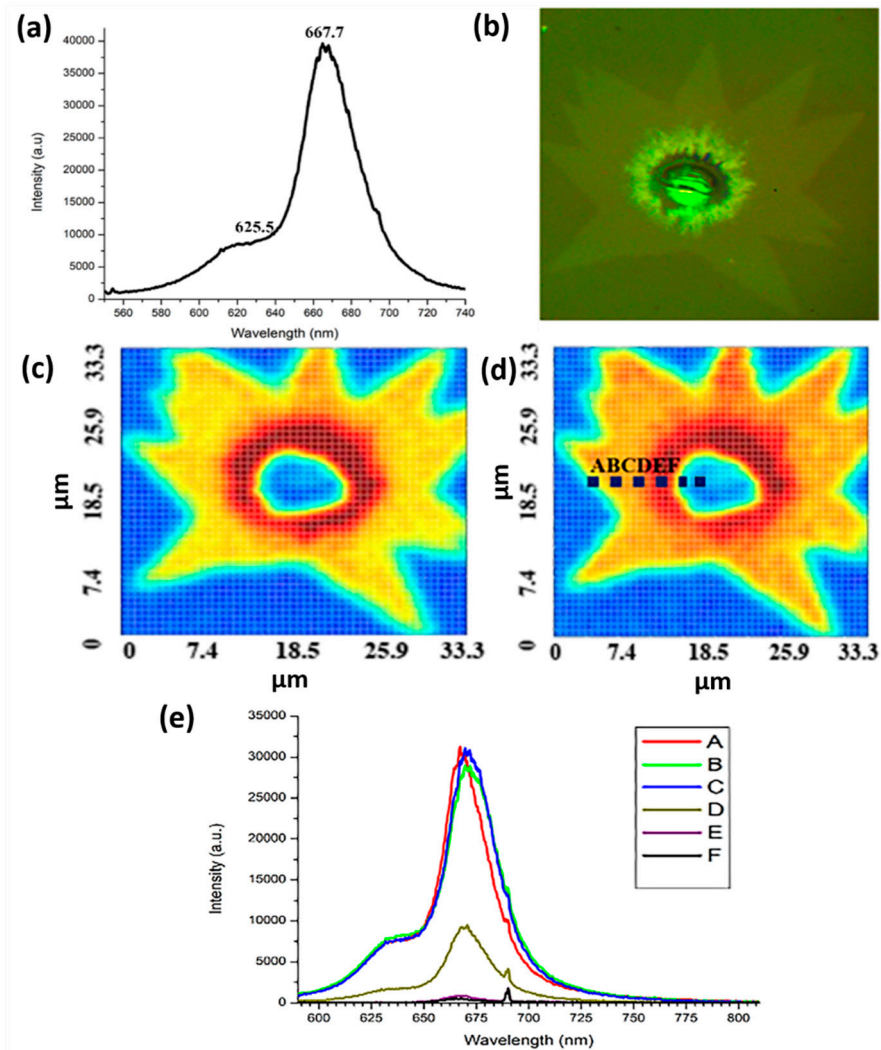
Figure 5. (**a**) PL measurement results of MoS$_2$ sample. (**b**) OM image of the selected PL mapping range. (**c,d**) PL mapping at 625 and 667 nm. (**e**) PL measurement result of the test piece marked by the blue dotted line in (**d**).

3.1.4. Selected Area Electron Diffraction

From the composition analysis, we can infer the mechanism of the periodic growth of MoS$_2$. We use the additional function of the TEM system to convert the diffraction image of the selected area into a lattice arrangement through FFT. The red line in Figure 6a indicates the FIB sampling position (see Supplementary Materials Section 2.5 for dual-beam FIB). Figure 6g is the SAED image of Figure 6d, with a miller index of [001]. In this direction, we can see the multilayer-structured MoS$_2$ lattice array. The distance between the layers reveals the hexagonal crystal structure of MoS$_2$ with lattice constants a = 0.318 nm and c = 1.299 nm. Moreover, the crystal plane distance between the multilayer MoS$_2$ layer is 6.2 A, which is close to the 2-H MoS$_2$ crystal plane distance of about 6.5 A. Figure 6h is the SAED image of Figure 6e. The miller index is [001], which shows that the lattice arrangement is chaotic, but the faint lattice points in the four directions may be MoO$_3$. Figure 6i is the SAED image of Figure 6f. The miller index is still [001], and the selected area is the junction of the mixed area and the sapphire substrate at the obvious double layer of HRTEM. Given that the boundary may diffract from the lattice of the upper and lower components of the boundary, it is more mixed. However, from the center point, the miller index [001] can be found, and the distance between the crystal planes is calculated to be about 6.4 Å.
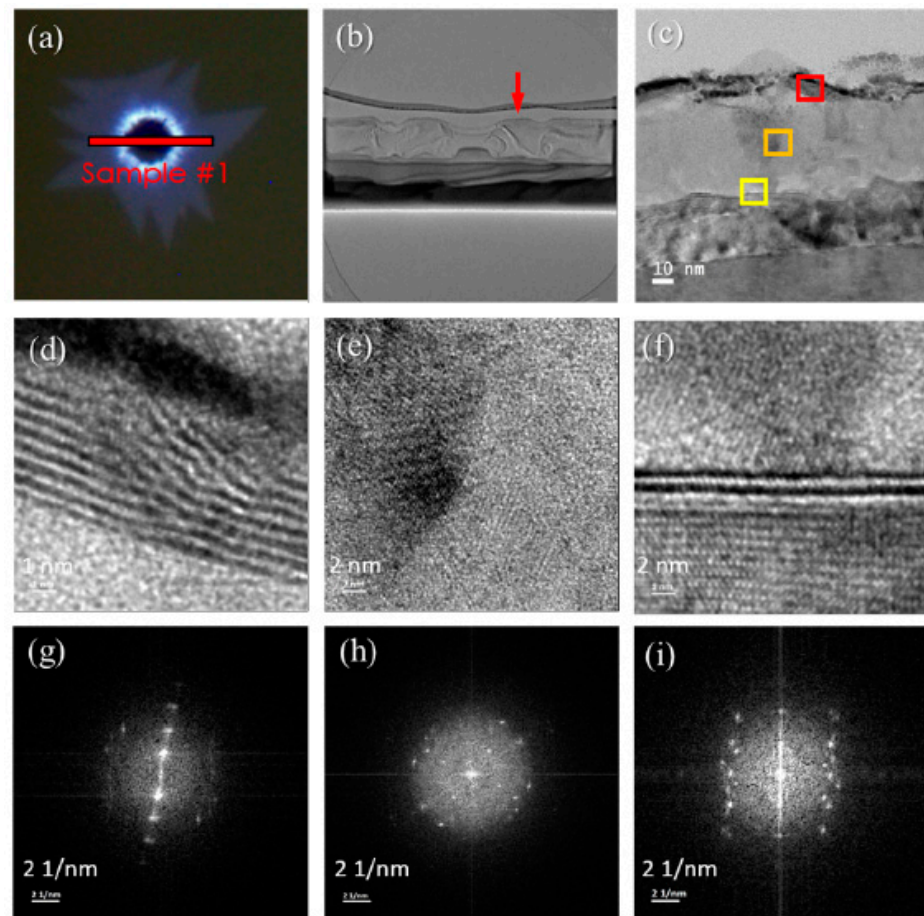
Figure 6. Panel (**a**) is the OM image after growing MoS_2, (**b**) is the cross-sectional TEM image of the selected area in (**a**), (**c**) is the enlarged TEM image of the red arrow in (**b**). Panels (**d**–**f**) represent the HRTEM images of the red, orange, and yellow boxes in (**c**), respectively, and (**g**–**i**) represent the SAED diagrams in (**d**–**f**), respectively.

Sample 2 is analyzed using the TEM image defined in Figure 7. The sampling position does not pass through the hole. The growth of MoS_2 on the surface is analyzed, as shown in Figure 7. Figure 7a shows the TEM image of the Sample 2 sampling location A, and the red box is the sampling location mark. Figure 7b shows the TEM image of the Sample 2 sampling location B, and the orange box is the sampling location mark. Figure 7c shows the TEM image of the Sample 2 sampling location C, and the yellow box is the sampling location mark. Figure 7d shows the HRTEM image of the red box in Figure 7a. The multilayer growth of MoS_2 is stacked layer by layer. Figure 7e shows the HRTEM image, where the orange box in Figure 7b is a mixed area, and no MoS_2 is observed. Figure 7f is the yellow box in Figure 7c. In the HRTEM image, the mixed zone is shown in the image. Figure 7g is the SAED diagram of Figure 7d, and the miller index is [001]. Here, the lattice arrangement can be seen as multilayer MoS_2. Figure 7h is the SAED diagram of Figure 7e. The miller index is [001], and the main composition seen is MoO_3. Figure 7i is the SAED diagram of Figure 7f, and the miller index is [001]. The image diffracted from the single-layer MoS_2 viewed from this miller index is a lattice point, which may be interpreted as a single-layer MoS_2 lattice. Based on the results of the SAED diagram analysis, we can determine from the lattice array that the grown MoS_2 material is consistent with the compound calculated using the element ratio. We can interpret that 2-H MoS_2 forms under the growth mechanism.
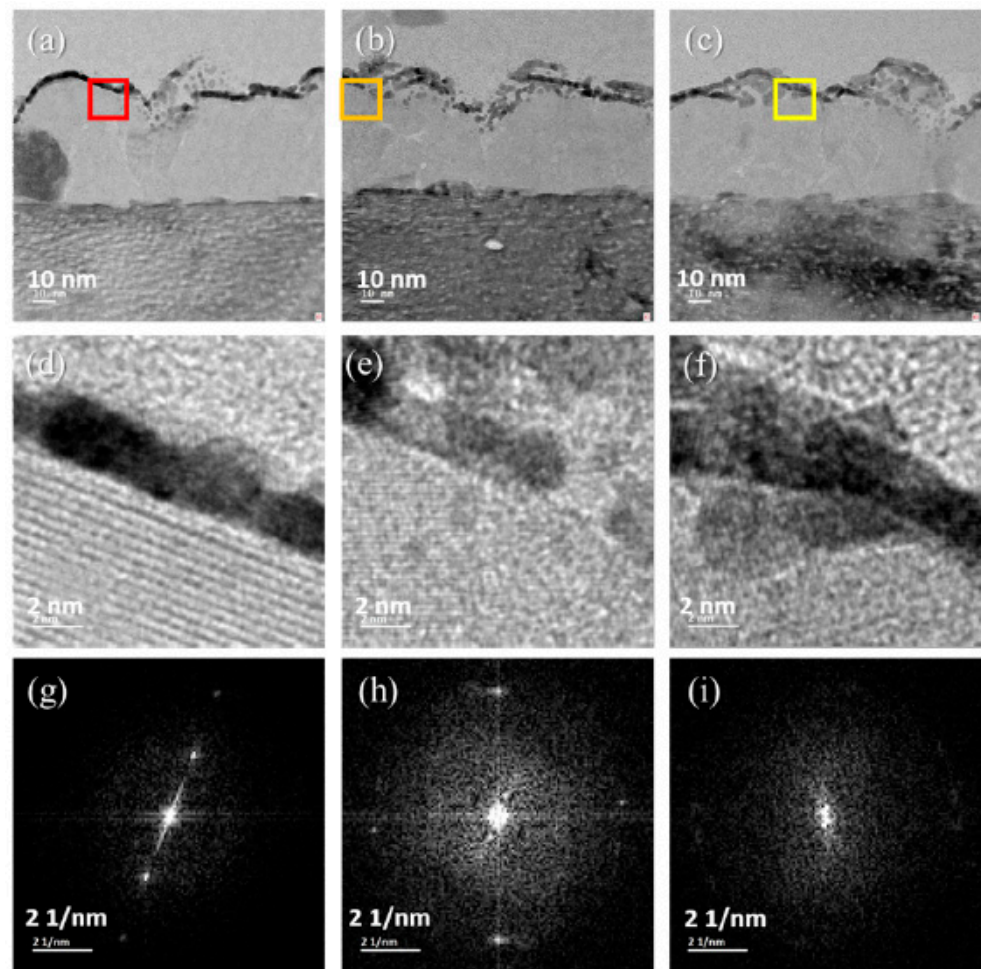
Figure 7. Panels (**a**–**c**) represent the TEM images of Sample 2 in sampling locations A, B, and C, respectively; (**d**–**f**) represent the HRTEM images of the red, orange, and yellow boxes in (**a**–**c**), respectively; and (**g**–**i**) represent the SAED diagram in (**d**–**f**), respectively.

4. Discussion

Figure 8 is a flow chart of the MoS_2 growth process with periodic holes. Figure 8a shows the surface undulation curve of the substrate with periodic holes on ungrown MoS_2. The blue line at the top of Figure 8b is the initial stage of growth. A single layer of MoS_2 forms when S is dominant, and the purple arrow above represents the direction of Ar. The light brown area in Figure 8c is the mixed region generated when MoO_3 is dominated. The composition contains Al_2O_3, MoO_3, and MoS_2. Figure 8d shows that when S becomes dominant during the growth period, a single layer or multiple layers of MoS_2 are deposited. Although MoS_2 grows and overlaps in a curved sheet shape, on the steeper edge of the hole, the sheet-shaped MoS_2 grows with the growth side facing upward. In Figure 8e, the brown dashed line indicates the mixed area covered by MoO_3 once again during the growth period. Figure 8f is the schematic at the end of the growth. The line segment overlapping on the top represents multiple layers. MoS_2 particles overlap with one another in a flake shape. The air flow is thicker after the hole in the direction than before the hole, as seen from the MoS_2 on the top. Finally, MoO_3 is nearly depleted, and S eventually dominates the final stage of CVD growth. This phenomenon is related to the experimental setting of 0.003 and 1 g of S.
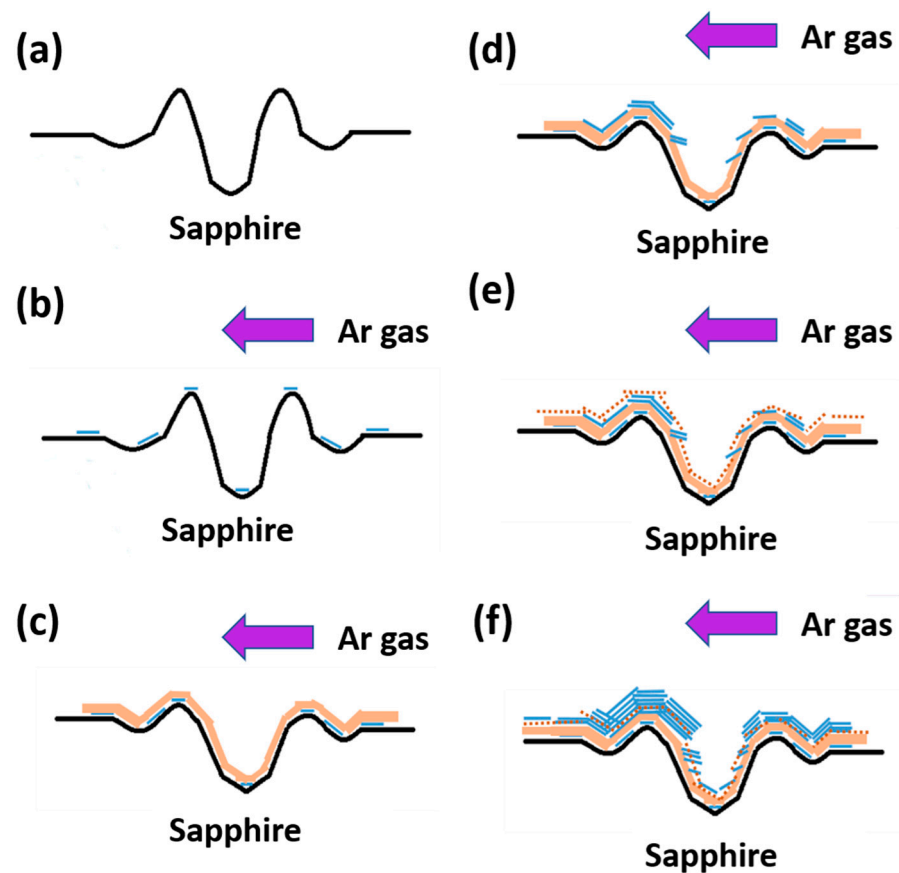
Figure 8. Schematic of the growth process of MoS_2. The purple arrow in the figure is the direction of argon ventilation, the blue line segment represents a single layer of MoS_2, the light yellow area represents the mixed zone dominated by MoO_3, the dark yellow dot is amorphous Al_2O_3 mixed in the reflection, and the blue line segment is superimposed to represent multilayer MoS_2.

Figure 9 is a schematic of the growth process of MoS_2, and Figure 9a is a schematic before growth. The upper layer of the lower sapphire substrate is an amorphous state damaged by laser processing. In Figure 9b, the blue arrow indicates the single layer of MoS_2 grown on the substrate surface at the initial stage of growth. In Figure 9c, the blue arrow indicates the coverage of MoO_3 at the middle stage of growth, and the green arrow indicates the Al_2O_3 surface layer at the same time, showing that it mixed at a high temperature to form a mixture zone. The blue arrow in Figure 9d indicates the formation of multiple layers of MoS_2, indicating that S gas is greater than MoO_3 gas during this growth period. Figure 9e is the schematic of the growth end, and the blue arrow indicates that multiple layers of MoS_2 grow to be stacked in sheets. Although in this study, MoS_2 is grown on a laser-processed periodic-hole sapphire substrate through CVD, to integrate the developed MoS_2 films into practical tools and nanostructures, various patterning and interfacing approaches have been developed. Post-patterning approaches have been successful, indicating wide-ranging applications in current microelectronic techniques, such as FIB milling, photo- and electron-beam lithography, and combinations of metal sputtering processes with selective etching after photolithographically defined masking [51–54].
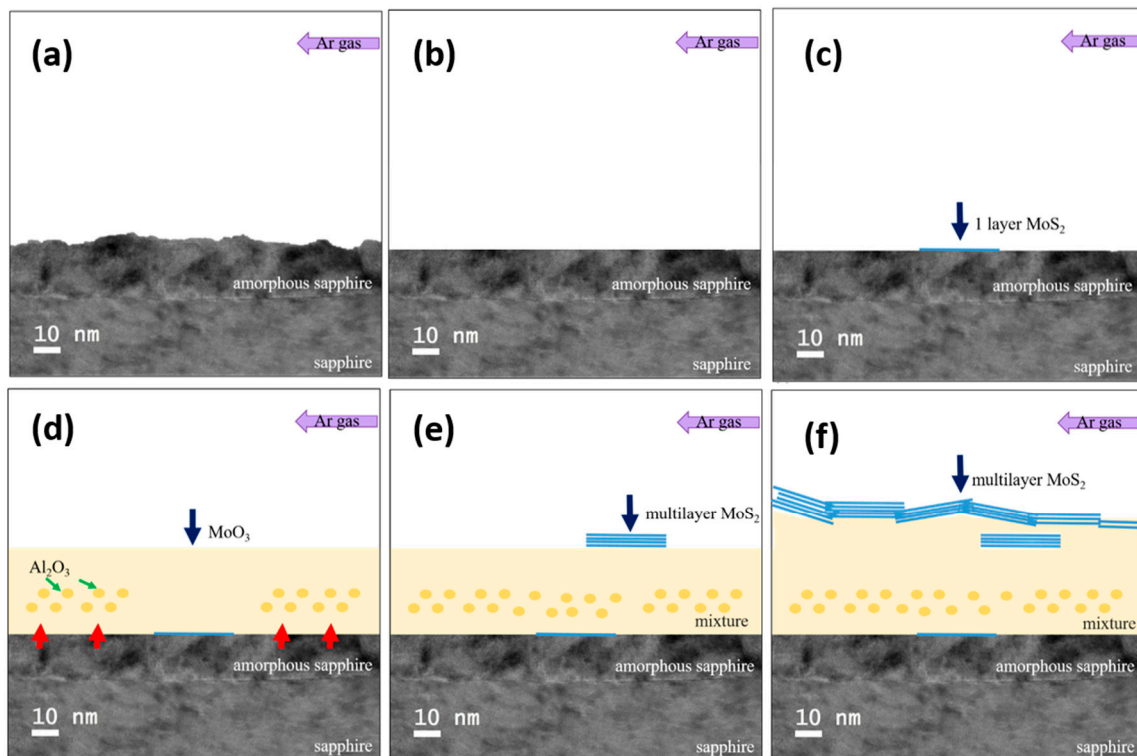
Figure 9. Schematic of the MoS$_2$ growth process. The purple arrow in the figure is the direction of argon ventilation, and the blue line segment represents a single layer of MoS$_2$. The light yellow area represents the mixed zone dominated by MoO$_3$, the dark yellow dot is amorphous Al$_2$O$_3$ mixed in the reflection, and the blue line segment is superimposed to represent multilayer MoS$_2$.

5. Conclusions

We used a femtosecond laser to prepare a periodic array of holes with a diameter of about 10 μm on a single-sided polished sapphire substrate. The substrate is grown by CVD of MoS$_2$, and the layer is successfully grown. This technique can be used for growth multiple times, and the results reveal that the size, shape, and number of layers of MoS$_2$ grown each time are different. The possible reason is that the experiment proceeds under atmospheric pressure. Creating a system completely isolated from external interference is impossible, and the influence of external environmental factors on the growth results cannot be predicted. However, other possible causes can be minimized by cleaning the experimental cavity, as well as ensuring minimal differences in parameters and the distance between each substrate installation. The growth mechanism is observed and analyzed using Raman, PL, and AFM analyses to confirm the distribution of the number of generated layers. They are found to possess single- and few-layer positions with excellent photoelectric and semiconductor properties. TEM is used to observe and analyze the cross-sectional image, and the extended function of the TEM is adopted to analyze and convert the SAED image. Subsequently, the growth mechanism is comprehensively analyzed. From the results, we can infer that in a large area of the substrate, MoS$_2$ growth increases and breaks with the direction of Ar until it is concentrated and periodically attaches around the holes, but not at the very end. For the same periodic hole in a small area, MoS$_2$ growth occurs by overlapping pieces, and the number of layers is distributed from the thickest ring around the hole to the single layer at the corner of MoS$_2$. After understanding this growth mechanism, we can select the part of the substrate to be used and the number of layers of MoS$_2$ according to the requirements of the components to be manufactured.

References

1. Geim, A.K.; Novoselov, K.S. The rise of graphene. *Nat. Mater.* **2007**, *6*, 183–191. [CrossRef]
2. Das Sarma, S.; Adam, S.; Hwang, E.H.; Rossi, E. Electronic transport in two-dimensional graphene. *Rev. Mod. Phys.* **2011**, *83*, 407–470. [CrossRef]
3. Lin, X.; Su, L.; Si, Z.; Zhang, Y.; Bournel, A.; Zhang, Y.; Klein, J.-O.; Fert, A.; Zhao, W. Gate-Driven Pure Spin Current in Graphene. *Phys. Rev. Appl.* **2017**, *8*, 034006. [CrossRef]
4. Wu, C.; Zhang, J.; Tong, X.; Yu, P.; Xu, J.Y.; Wu, J.; Wang, Z.M.; Lou, J.; Chueh, Y.L. A critical review on enhancement of photocatalytic hydrogen production by molybdenum disulfide: From growth to interfacial activities. *Small* **2019**, *15*, 1900578. [CrossRef] [PubMed]
5. Yang, D.; Wang, H.; Luo, S.; Wang, C.; Zhang, S.; Guo, S. Cut Flexible Multifunctional Electronics Using MoS$_2$ Nanosheet. *Nanomaterials* **2019**, *9*, 922. [CrossRef]
6. Zhang, Y.; Wan, Q.; Yang, N. Recent Advances of Porous Graphene: Synthesis, Functionalization, and Electrochemical Applications. *Small* **2019**, *15*, 1903780. [CrossRef]
7. Li, K.-C.; Lu, M.-Y.; Nguyen, H.T.; Feng, S.-W.; Artemkina, S.B.; Fedorov, V.E.; Wang, H.-C. Intelligent Identification of MoS$_2$ Nanostructures with Hyperspectral Imaging by 3D-CNN. *Nanomaterials* **2020**, *10*, 1161. [CrossRef]
8. Choi, M.S.; Lee, G.-H.; Yu, Y.-J.; Lee, D.-Y.; Lee, S.H.; Kim, P.; Hone, J.; Yoo, W.J. Controlled charge trapping by molybdenum disulphide and graphene in ultrathin heterostructured memory devices. *Nat. Commun.* **2013**, *4*, 1624. [CrossRef]
9. Han, T.; Liu, H.; Wang, S.; Chen, S.; Xie, H.; Yang, K. Probing the Field-Effect Transistor with Monolayer MoS$_2$ Prepared by APCVD. *Nanomaterials* **2019**, *9*, 1209. [CrossRef]

10. Lee, C.H.; Lee, G.H.; Van Der Zande, A.M.; Chen, W.; Li, Y.; Han, M.; Cui, X.; Arefe, G.; Nuckolls, C.; Heinz, T.F.; et al. Atomically thin p–n junctions with van derWaals heterointerfaces. *Nat. Nanotechnol.* **2014**, *9*, 676–681. [CrossRef] [PubMed]

11. Lu, G.Z.; Wu, M.J.; Lin, T.N.; Chang, C.Y.; Lin, W.L.; Chen, Y.T.; Hou, C.F.; Cheng, H.J.; Lin, T.Y.; Shen, J.L.; et al. Electrically Pumped White-Light-Emitting Diodes Based on Histidine-Doped MoS_2 Quantum Dots. *Small* **2019**, *15*, 1901908. [CrossRef] [PubMed]

12. Park, Y.J.; Sharma, B.K.; Shinde, S.M.; Kim, M.-S.; Jang, B.; Kim, J.-H.; Ahn, J.-H. All MoS_2-Based Large Area, Skin-Attachable Active-Matrix Tactile Sensor. *ACS Nano* **2019**, *13*, 3023–3030. [CrossRef] [PubMed]

13. Radisavljevic, B.; Radenovic, A.; Brivio, J.; Giacometti, V.; Kis, A. Single-layer MoS_2 transistors. *Nat. Nanotechnol.* **2011**, *6*, 147–150. [CrossRef]

14. Roh, J.; Ryu, J.H.; Baek, G.W.; Jung, H.; Seo, S.G.; An, K.; Jeong, B.G.; Lee, D.C.; Hong, B.H.; Bae, W.K.; et al. Threshold Voltage Control of Multilayered MoS_2 Field-Effect Transistors via Octadecyltrichlorosilane and their Applications to Active Matrixed Quantum Dot Displays Driven by Enhancement-Mode Logic Gates. *Small* **2019**, *15*, 1803852. [CrossRef] [PubMed]

15. Zhao, J.; Li, N.; Yu, H.; Wei, Z.; Liao, M.; Chen, P.; Wang, S.; Shi, D.; Sun, Q.; Zhang, G. Highly Sensitive MoS_2 Humidity Sensors Array for Noncontact Sensation. *Adv. Mater.* **2017**, *29*, 1702076. [CrossRef]

16. Zhang, P.; Yang, S.; Pineda-Gómez, R.; Ibarlucea, B.; Ma, J.; Lohe, M.R.; Akbar, T.F.; Baraban, L.; Cuniberti, G.; Feng, X. Electrochemically Exfoliated High-Quality 2H-MoS_2 for Multiflake Thin Film Flexible Biosensors. *Small* **2019**, *15*, 1901265. [CrossRef] [PubMed]

17. Yang, K.; Liu, H.; Wang, S.; Li, W.; Han, T. A horizontal-gate monolayer MoS_2 transistor based on image force barrier reduction. *Nanomaterials* **2019**, *9*, 1245. [CrossRef]

18. Yadav, V.; Roy, S.; Singh, P.; Khan, Z.; Jaiswal, A. 2D MoS_2-Based Nanomaterials for Therapeutic, Bioimaging, and Biosensing Applications. *Small* **2019**, *15*, 1803706. [CrossRef]

19. Shin, M.; Yoon, J.; Yi, C.; Lee, T.; Choi, J.-W. Flexible HIV-1 Biosensor Based on the Au/MoS_2 Nanoparticles/Au Nanolayer on the PET Substrate. *Nanomaterials* **2019**, *9*, 1076. [CrossRef]

20. Sarkar, D.; Liu, W.; Xie, X.; Anselmo, A.C.; Mitragotri, S.; Banerjee, K. MoS_2 Field-Effect Transistor for Next-Generation Label-Free Biosensors. *ACS Nano* **2014**, *8*, 3992–4003. [CrossRef]

21. Zhu, L.; Ji, J.; Liu, J.; Mine, S.; Matsuoka, M.; Zhang, J.; Xing, M. Designing 3D-MoS_2 Sponge as Excellent Cocatalysts in Advanced Oxidation Processes for Pollutant Control. *Angew. Chem. Int. Ed.* **2020**, *59*, 13968–13976. [CrossRef] [PubMed]

22. Zheng, L.; Han, S.; Liu, H.; Yu, P.; Fang, X. Hierarchical MoS_2 nanosheet@ TiO_2 nanotube array composites with enhanced photocatalytic and photocurrent performances. *Small* **2016**, *12*, 1527–1536. [CrossRef]

23. Ali, M.B.; Jo, W.K.; Elhouichet, H.; Boukherroub, R. Reduced graphene oxide as an efficient support for CdS-MoS_2 heterostructures for enhanced photocatalytic H_2 evolution. *Int. J. Hydrogen Energy* **2017**, *42*, 16449–16458.

24. Li, H.; Yu, K.; Tang, Z.; Fu, H.; Zhu, Z. High photocatalytic performance of a type-II α-MoO_3@ MoS_2 heterojunction: From theory to experiment. *Phys. Chem. Chem. Phys.* **2016**, *18*, 14074–14085. [CrossRef]

25. Zhang, X.; Yang, Y.; Ding, S.; Que, W.; Zheng, Z.; Du, Y. Construction of High-Quality SnO_2@MoS_2 Nanohybrids for Promising Photoelectrocatalytic Applications. *Inorg. Chem.* **2017**, *56*, 3386–3393. [CrossRef]

26. Mak, K.F.; Lee, C.; Hone, J.; Shan, J.; Heinz, T.F. Atomically Thin MoS_2: A New Direct-Gap Semiconductor. *Phys. Rev. Lett.* **2010**, *105*, 136805. [CrossRef]

27. Splendiani, A.; Sun, L.; Zhang, Y.; Li, T.; Kim, J.; Chim, C.-Y.; Galli, G.; Wang, F. Emerging Photoluminescence in Monolayer MoS_2. *Nano Lett.* **2010**, *10*, 1271–1275. [CrossRef] [PubMed]

28. Liu, H.F.; Wong, S.L.; Chi, D.Z. CVD Growth of MoS_2-based Two-dimensional Materials. *Chem. Vap. Depos.* **2015**, *21*, 241–259. [CrossRef]

29. Tongay, S.; Fan, W.; Kang, J.; Park, J.; Koldemir, U.; Suh, J.; Narang, D.S.; Liu, K.; Ji, J.; Li, J.; et al. Tuning Interlayer Coupling in Large-Area Heterostructures with CVD-Grown MoS_2 and WS_2 Monolayers. *Nano Lett.* **2014**, *14*, 3185–3190. [CrossRef]

30. Perea-Lopez, N.; Lin, Z.; Pradhan, N.R.; Iñiguez-Rábago, A.; Elías, A.L.; McCreary, A.; Lou, J.; Ajayan, P.M.; Terrones, H.; Balicas, L.; et al. CVD-grown monolayered MoS_2 as an effective photosensor operating at low-voltage. *2D Mater.* **2014**, *1*, 011004. [CrossRef]

31. Cunningham, P.D.; McCreary, K.M.; Hanbicki, A.T.; Currie, M.; Jonker, B.T.; Hayden, L.M. Charge trapping and exciton dyanamics in large-area CVD grown MoS_2. *J. Phys. Chem. C* **2016**, *120*, 5819–5826. [CrossRef]

32. Zhang, W.; Huang, J.-K.; Chen, C.-H.; Chang, Y.-H.; Cheng, Y.-J.; Li, L.-J. High-Gain Phototransistors Based on a CVD MoS_2 Monolayer. *Adv. Mater.* **2013**, *25*, 3456–3461. [CrossRef] [PubMed]

33. Chae, W.H.; Cain, J.D.; Hanson, E.D.; Murthy, A.A.; Dravid, V.P. Substrate-induced strain and charge doping in CVD-grown monolayer MoS_2. *Appl. Phys. Lett.* **2017**, *111*, 143106. [CrossRef]

34. Kondekar, N.; Boebinger, M.G.; Tian, M.; Kirmani, M.H.; McDowell, M.T. The Effect of Nickel on MoS_2 Growth Revealed with in Situ Transmission Electron Microscopy. *ACS Nano* **2019**, *13*, 7117–7126. [CrossRef] [PubMed]

35. Eijsbouts, S.; Heinerman, J.; Elzerman, H. MoS_2 structures in high-activity hydrotreating catalysts: I. Semi-quantitative method for evaluation of transmission electron microscopy results. Correlations between hydrodesulfurization and hydrodenitrogenation activities and MoS_2 dispersion. *Appl. Catal. A Gen.* **1993**, *105*, 53–68. [CrossRef]

36. Zeng, Z.; Zhang, X.; Bustillo, K.; Niu, K.; Gammer, C.; Xu, J.; Zheng, H. In Situ Study of Lithiation and Delithiation of MoS_2 Nanosheets Using Electrochemical Liquid Cell Transmission Electron Microscopy. *Nano Lett.* **2015**, *15*, 5214–5220. [CrossRef]

37. Tai, K.L.; Huang, C.W.; Cai, R.F.; Huang, G.M.; Tseng, Y.T.; Chen, J.; Wu, W.W. Atomic-scale fabrication of in-plane heterojunctions of few-layer MoS$_2$ via in situ scanning transmission electron microscopy. *Small* **2020**, *16*, 1905516. [CrossRef]

38. Wang, M.; Kim, J.H.; Han, S.S.; Je, M.; Gil, J.; Noh, C.; Ko, T.-J.; Lee, K.S.; Son, D.I.; Bae, T.-S.; et al. Structural Evolutions of Vertically Aligned Two-Dimensional MoS$_2$ Layers Revealed by in Situ Heating Transmission Electron Microscopy. *J. Phys. Chem. C* **2019**, *123*, 27843–27853. [CrossRef]

39. Lahouij, I.; Vacher, B.; Dassenoy, F. Direct observation by in situ transmission electron microscopy of the behaviour of IF-MoS$_2$ nanoparticles during sliding tests: Influence of the crystal structure. *Lubr. Sci.* **2014**, *26*, 163–173. [CrossRef]

40. Chen, Y.-S.; Liao, C.-H.; Chueh, Y.-L.; Lai, C.-C.; Chen, L.-Y.; Chu, A.-K.; Kuo, C.-T.; Wang, H.-C. High performance Cu$_2$O/ZnO core-shell nanorod arrays synthesized using a nanoimprint GaN template by the hydrothermal growth technique. *Opt. Mater. Express* **2014**, *4*, 1473–1486. [CrossRef]

41. Li, F.; Shen, T.; Xu, L.; Hu, C.; Qi, J. Strain Improving the Performance of a Flexible Monolayer MoS$_2$ Photodetector. *Adv. Electron. Mater.* **2019**, *5*, 1900803. [CrossRef]

42. Shree, S.; George, A.; Lehnert, T.; Neumann, C.; Benelajla, M.; Robert, C.; Marie, X.; Watanabe, K.; Taniguchi, T.; Kaiser, U.; et al. High optical quality of MoS$_2$ monolayers grown by chemical vapor deposition. *2D Mater.* **2019**, *7*, 015011. [CrossRef]

43. Dong, X.; Dong, J.; Yetisen, A.K.; Köhler, M.H.; Wang, S.; Jakobi, M.; Koch, A.W. Characterization and layer thickness mapping of two-dimensional MoS$_2$ flakes via hyperspectral line-scanning microscopy. *Appl. Phys. Express* **2019**, *12*, 102004. [CrossRef]

44. Li, P.; Zhang, D.; Wu, Z. Flexible MoS$_2$ sensor arrays for high performance label-free ion sensing. *Sens. Actuators A Phys.* **2019**, *286*, 51–58. [CrossRef]

45. Zhang, D.; Yang, Z.; Li, P.; Pang, M.; Xue, Q. Flexible self-powered high-performance ammonia sensor based on Au-decorated MoSe$_2$ nanoflowers driven by single layer MoS$_2$-flake piezoelectric nanogenerator. *Nano Energy* **2019**, *65*, 103974. [CrossRef]

46. Dorn, M.; Lange, P.; Chekushin, A.; Severin, N.; Rabe, J.P. High contrast optical detection of single graphenes on optically transparent substrates. *J. Appl. Phys.* **2010**, *108*, 106101. [CrossRef]

47. Wang, H.-C.; Huang, S.-W.; Yang, J.-M.; Wu, G.-H.; Hsieh, Y.-P.; Feng, S.-W.; Lee, M.K.; Kuo, C.-T. Large-area few-layered graphene film determination by multispectral imaging microscopy. *Nanoscale* **2015**, *7*, 9033–9039. [CrossRef] [PubMed]

48. Lu, M.-Y.; Wu, S.-C.; Wang, H.-C.; Lu, M.P. Time-evolution of the electrical characteristics of MoS$_2$ field-effect transistors after electron beam irradiation. *Phys. Chem. Chem. Phys.* **2018**, *20*, 9038–9044. [CrossRef]

49. Hsieh, Y.-P.; Wang, Y.-W.; Ting, C.-C.; Wang, H.-C.; Chen, K.-Y.; Yang, C.-C. Effect of Catalyst Morphology on the Quality of CVD Grown Graphene. *J. Nanomater.* **2013**, *2013*, 6. [CrossRef]

50. Wu, I.-C.; Weng, Y.-H.; Lu, M.-Y.; Jen, C.-P.; Fedorov, V.; Chen, W.C.; Wu, M.-T.; Kuo, C.-T.; Wang, H.-C. Nano-structure ZnO/Cu$_2$O photoelectrochemical and self-powered biosensor for esophageal cancer cell detection. *Opt. Express* **2017**, *25*, 7689–7706. [CrossRef]

51. Li, H.; Li, P.; Huang, J.-K.; Li, M.-Y.; Yang, C.-W.; Shi, Y.; Zhang, X.-X.; Li, L.-J. Laterally Stitched Heterostructures of Transition Metal Dichalcogenide: Chemical Vapor Deposition Growth on Lithographically Patterned Area. *ACS Nano* **2016**, *10*, 10516–10523. [CrossRef] [PubMed]

52. Han, G.H.; Kybert, N.J.; Naylor, C.H.; Lee, B.S.; Ping, J.; Park, J.H.; Johnson, A.C. Seeded growth of highly crystalline molybdenum disulphide monolayers at controlled locations. *Nat. Commun.* **2015**, *6*, 6128. [CrossRef] [PubMed]

53. Jung, Y.; Shen, J.; Sun, Y.; Cha, J.J. Chemically synthesized heterostructures of two-dimensional molybdenum/tungsten-based dichalcogenides with vertically aligned layers. *ACS Nano* **2014**, *8*, 9550–9557. [CrossRef] [PubMed]

54. Pareek, D.; Roach, K.G.; Gonzalez, M.A.; Büsing, L.; Parisi, J.; Gütay, L.; Schäfer, S. Micro-patterned deposition of MoS$_2$ ultrathin-films by a controlled droplet dragging approach. *Sci. Rep.* **2021**, *11*, 13993. [CrossRef]